Chapter 8

Excitation of C_{60}

The response of C_{60} fullerenes upon excitation with intense pulsed laser radiation can be investigated by photoion and photoelectron spectroscopy. A laser pulse duration of down to $9\,\text{fs}$ allows one to study excitation mechanisms on a time scale below the characteristic time scales for electron-electron and electron-phonon coupling. Thus, it is possible to separate the energy deposition into the system from the energy redistribution among the various electronic and nuclear degrees of freedom in time. Moreover, single pulse experiments as a function of laser parameters such as pulse duration, intensity, and/or ellipticity provide a powerful tool for to explore the energy flow in C_{60} at moderately strong laser intensities ($< 10^{15}\,\text{W/cm}^2$).

This chapter begins with a brief discussion of multiphoton ionisation of C_{60} fullerenes. Then the experimental results are reported, starting with single pulse excitation at different pulse duration and intensities, followed by ellipticity dependent studies using photoion and photoelectron spectroscopy.

8.1 Multiphoton Ionisation of C_{60}

8.1.1 Different Ionisation Mechanisms

Various systematic studies on multiphoton ionisation (MPI) of C_{60} fullerenes with different laser parameters have been performed recently [THD00, CHH01, CHR01]. It was found that the ionisation behaviour of C_{60} depends strongly on the laser pulse duration τ [CHH00]. Depending on the excitation time scale three different ionisation mechanisms were identified. For very short pulses ($\tau < 70\,\text{fs}$) the excitation energy tends to remain in the electronic system

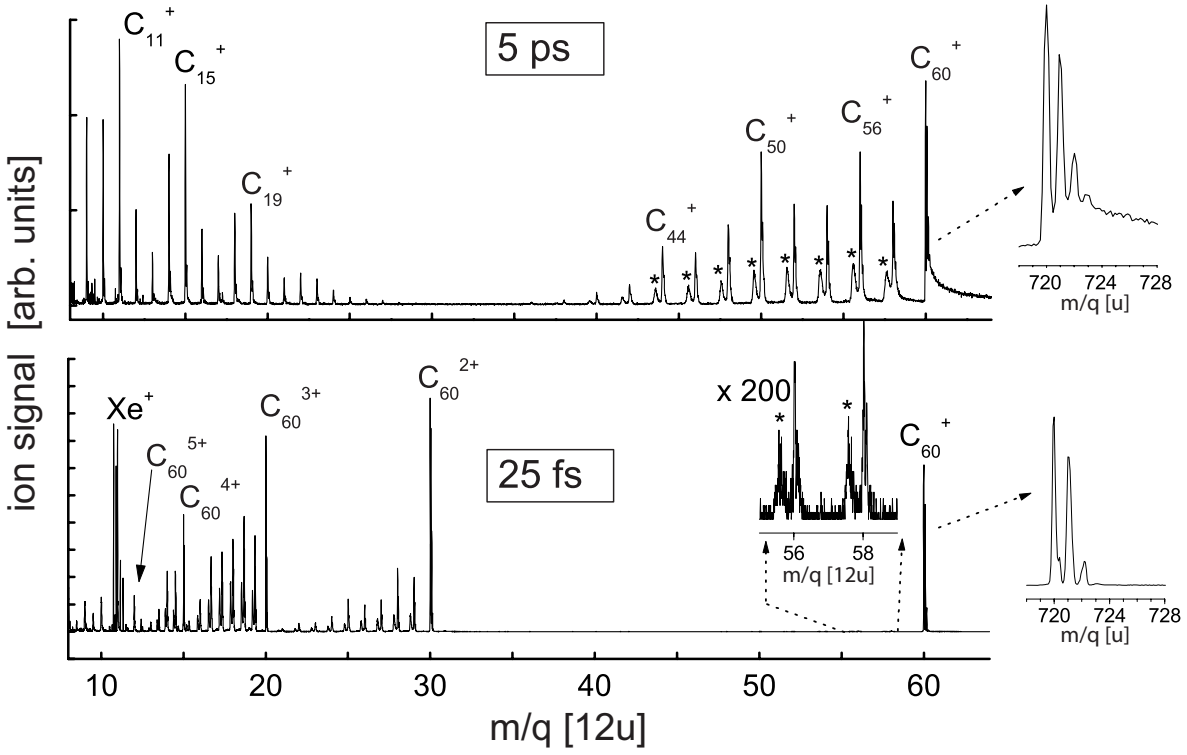

Figure 8.1: Typical mass spectra of C_{60} produced by laser pulses of 795 nm wavelength with a pulse duration of 5 ps (top) and 25 fs (bottom) (the picture is taken from [HLS05]). The spectra were recorded at roughly equal laser fluences, the corresponding intensities being 3.2×10^{12} W/cm² and 1.0×10^{15} W/cm², respectively.

with relatively little vibrational heating of nuclear motion. Thus, multiply charged C_{60} ions formed by direct multiphoton ionisation are observed. For longer laser pulses ($\tau <$ ps) the absorbed energy is coupled among electronic degrees of freedom and the ionisation becomes of thermal nature. Finally, for very long pulses ($\tau >$ ps) electron-phonon coupling leads to massive fragmentation and delayed ionisation. As an example Fig. 8.1 illustrates the substantial differences observed in mass spectra when the laser pulse duration is changed from 25 fs to 5 ps. Both spectra were recorded at roughly equal laser fluences of ≈ 22 J/cm^2 which corresponds to intensities of 1.0×10^{15} W/cm^2 ($\tau = 25$ fs) and 3.2×10^{12} W/cm^2 ($\tau = 5$ ps). The mass spectrum obtained with a pulse duration of 25 fs exhibits a strong contribution of multiply charged C_{60}^{q+} ions and from corresponding large, fullerene-like fragments which are formed by sequential C_2 losses. However, only a limited number of singly charged fragments is detected, as shown in the enlarged insert. On the other hand, the mass spectrum recorded upon interaction with 5 ps pulses resembles very much the typical bimodal mass distribution

observed in ns experiments [KHO85]. Here only singly charged ions and various fragments are observed. In addition, the enlarged insert shows a significant tail on the higher delay time side of the C_{60}^+ mass peak, originating from delayed ionisation explained in see Sec. 3.2. Such a tail is not visible in the case of excitation with 25 fs pulses. The fraction of delayed ionisation increases almost linearly with laser pulse duration [HLS05].

In both cases (excitation with 25 fs and 5 ps laser pulses), peaks originating from metastable statistical decay of highly vibrationally excited fullerene-like fragments on a μs-ms time scale [CLe00] are marked with asterisks. In this context some questions still remain open: how is the energy ≥ 40 eV needed for metastable fragmentation initially deposited into the system? Does the single active electron (SAE) dynamics, which prevails in strong field interactions with atomic systems, still dominate in a large molecular system over the intuitively more plausible many active electrons (MAE) response [LBI02, MSR03]?

8.1.2 Saturation Intensity

In a simple multiphoton picture the nonresonant ionisation rate W_N of C_{60} depends on the generalised multiphoton cross-section σ_N according to Eq. (3.7) as

$$W_N = \gamma_N I^N \quad , \tag{8.1}$$

where $\gamma_N = \sigma_N/(h\nu)^N$. Lacking any better knowledge[1], for simplicity in the following discussion σ_N is assumed to be independent of the laser intensity. In accordance with the considerations on the Rayleigh length (see Sec 6.2) the interaction with a cylindrically symmetric parallel Gaussian laser beam is assumed

$$I(r,t) = I_0 e^{-2\left(\frac{r}{w}\right)^2} e^{-4\ln 2\left(\frac{t}{\tau}\right)^2} \quad , \tag{8.2}$$

where $I(r,t)$ is the beam intensity at a given time t and distance r from the beam axis, I_0 is the peak pulse intensity, τ is the temporal FWHM, and w is the beam waist (radius at which the intensity drops down to $1/e^2$ with respect to its maximum value). The change of the target density $dn(r,t)$ at any given r and t is

$$dn(r,t) = -n(r,t)\gamma_N I^N(r,t)dt \quad . \tag{8.3}$$

[1] However, the ADK theory (see Sec. 3.2), with a number of shortcomings such as wavelength independence [TZL02], can be considered as an unproven alternative for such a molecular system.

Integration of Eq. (8.3) over the pulse durations gives

$$n(r) = n_0 \exp\left(-\gamma_N I_0^N \sqrt{\frac{\pi}{4\ln 2N}}\tau \exp\left[-2N\left(\frac{r}{w}\right)^2\right]\right) \quad , \tag{8.4}$$

where n_0 is the initial target density. By introducing the following substitutions $\beta^2 = 2N/w^2$ and $v^N = \gamma_N I_0^N \sqrt{\frac{\pi}{4\ln 2N}}\tau$ Eq. (8.4) can be rewritten in the form

$$n(r) = n_0 \exp\{-v^N \exp[-\beta^2 r^2]\} \quad . \tag{8.5}$$

Obviously, v is a dimensionless intensity parameter which can be expressed by

$$v = \frac{I_0}{I_{sat}} \quad , \tag{8.6}$$

where a "saturation intensity"[1] is defined as

$$I_{sat} = \left(\frac{1}{\gamma_N \tau}\sqrt{\frac{4\ln 2N}{\pi}}\right)^{1/N} \quad . \tag{8.7}$$

The saturation intensity I_{sat} determines the intensity at which the ionisation probability in the beam center $[n_0 - n(0)]/n_0$ becomes sufficiently large, i.e. $1-1/e$ or 63% (note, $n(r)/n_0$ can never becomes unity). Any further increase of the ion yield with intensity essentially originates from an increase of the interaction volume in which saturation is reached as I_0 is further increased. I_{sat} contains information about the multiphoton cross-section, the ionisation order, and its value depends on the laser pulse duration. Therefore, from Eq. (8.7) the following scaling law for saturation intensities as a function of the laser pulse duration can be deduced

$$I_{sat} \propto \frac{1}{\sqrt[N]{\tau}} \quad . \tag{8.8}$$

The measured total ion signal S is determined by the decrease of the initial target density $n_0 - n(r)$. The signal dS originating from a ring between r and $r + dr$ and a length l at a detection efficiency F is given by

$$dS = 2\pi n_0 F l r \left\{1 - \exp\left[-v^N \exp\left(-\beta^2 r^2\right)\right]\right\} dr \quad . \tag{8.9}$$

The total measured signal S is derived by integration of Eq. (8.9) over the whole Gaussian beam

$$S = \alpha n_0 [\Gamma + \ln v^N + E_1(v^N)] \quad , \tag{8.10}$$

[1] Note that this definition differs slightly from that of [HVC00]. In contrast to that work, however, an analytical expression for I_{sat} (based on the assumption of a strict power law according to Eq. (8.1)) is used here rather than a somewhat difficult to justify linear extrapolation of the semilogarithmically plotted experimental data.

where α is the proportionality constant, $\Gamma = 0.5772156649$ is the Euler constant, and $E_1(v^N)$ is the integral exponential function defined as

$$E_1(x) = \int_x^\infty (e^{-u}/u)du \quad . \tag{8.11}$$

In the present work Eq. (8.10) is used to fit the experimental data and to derive saturation intensities for different charge states q of C_{60}^{q+}. The approach of [HVC00] and [HVC01] already mentioned above to extract saturation intensities from experimental data leads to similar results. There the saturation intensity is obtained from the intersection of the recorded ion signal in a lin-log plot (linearly depending on $\ln I$) with the abscissa.

8.1.3 Ionisation Energy and Model Potential

The saturation intensities can be derived using a model potential of C_{60}^{q+} in the description of the ionisation process $C_{60}^{q+} \longrightarrow C_{60}^{(q+1)+}$ in the laser field. Here saturation is assumed to occur when the potential barrier falls below the ionisation energy of the respective charge state. Thus, values of the saturation intensities become sensitive to the ionisation potential (IP) and the model potential of the ionic core.

The available experimental data on the IPs for different charged states of C_{60} demonstrate a good reliability only for $q = 1$ [HSV92, SVK92, VSK92], while for $q = 2$ the experimental value is known with less accuracy [WDS94]. Also a number of theoretical works was dedicated to the IPs of C_{60}^{q+} [YLa94, TBF95, SVS96]. Recently, a linear dependence between the ionisation potential E_{IP} and the charge state q has been extracted from density-functional calculation [DAM05]

$$E_{IP} = 7.108 + 3.252q \quad . \tag{8.12}$$

This dependence is indicated by the dashed line in Fig. 8.2 together with IPs from the above mentioned experimental data (symbols). The theoretical calculation underestimates the experimental values. Therefore, a different linear equation with a somewhat larger slope and much better agreement to the experimental data is suggested, which is presented by the solid line in Fig. 8.2

$$E_{IP} = 7.6 + 4.248q \quad . \tag{8.13}$$

The second therm of Eq. (8.13) corresponds to the energy $qe^2/(4\pi\varepsilon_0 R_C)$ needed to remove an electron from the C_{60}^{q+} surface at radius R_C to infinity. The value R_C of 3.39 Å is used in

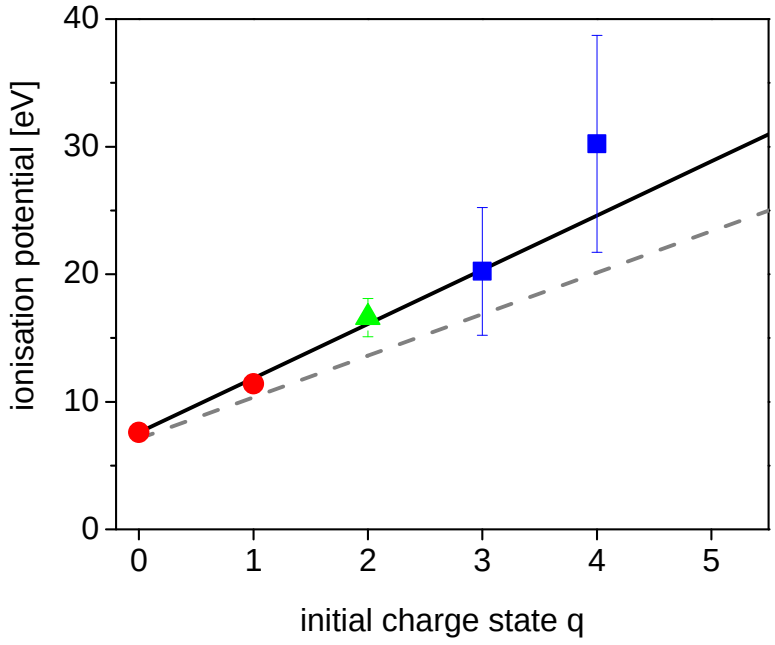

Figure 8.2: Ionisation potentials for different charge states of C_{60}^{q+}. Experimental values (symbols) are adopted from [HSV92, SVK92] (red circles), [WDS94] (green triangle), and [MER97] (blue squares). The data from [MER97] were originally reported for C_{70}^{q+}, therefore, these values have been corrected by a factor of 1.08 to account for the smaller diameter of C_{60}. The theoretical data taken from [DAM05] (grey dashed line) and calculated results according to Eq. (8.13) (black solid line) are also shown.

Eq. (8.13). This value is in reasonable agreement with the known mean radius 3.55 Å of C_{60} [DDE96].

For estimating saturation intensities the potential of the ionic core is modelled. Different models are discussed in the literature. Corkum et al. [BCR03] used a model based on charged, conducting, and polarisable sphere for C_{60}^{q+}. Alternatively, a more realistic jellium type potential was used in Ref. [PNi93]. An extended potential $V(r,q)$ based on the jellium type model, which is used in the present work, is given by the following expression

$$V(r,q) = \begin{cases} -2\exp\left(-r_0\left|r-r_0\right|\right) - \left|r-r_0\right|^{-1} - 0.14978(q-1) & \text{if} \quad r < 2.75 \\ -2\exp\left(-r_0\left|r-r_0\right|\right) - \left|r-r_0\right|^{-1} - h(r,q) & \text{if} \quad 2.75 \le r < 5.13 \\ -1.5\left(1+\exp\left(\left|r-r_0\right|-1.5580\right)/0.006\right)^{-1} + g(r,q) & \text{if} \quad 5.13 \le r < 5.15 \\ -1.5 + 0.012(r-r_0)^4 + g(r,q) & \text{if} \quad 5.15 \le r \le 8.23 \\ -1.5\left(1+\exp\left(\left|r-r_0\right|-1.5580\right)/0.006\right)^{-1} + g(r,q) & \text{if} \quad 8.23 < r \le 8.2497534 \\ -2\exp\left(-r_0\left|r-r_0\right|\right) - \left|r-r_0\right|^{-1} + g(r,q) & \text{if} \quad 8.2497534 < r \end{cases}, \tag{8.14}$$

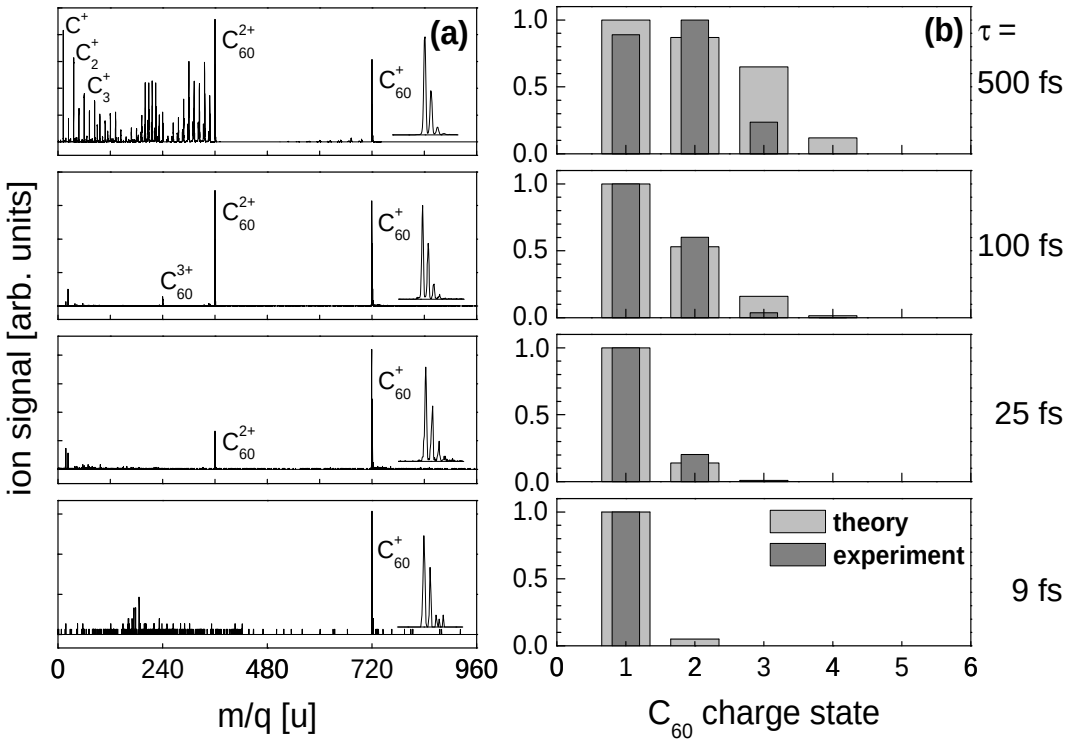

Figure 8.3: Comparison between experimental data of C_{60} photoionisation and the theoretical ionisation rates derived from S-matrix theory by A. Becker and F. H. M. Faisal: (a) mass spectra obtained with 797 fs laser pulses as a function of pulse durations at 4×10^{13} W/cm^2 (the upper three spectra are reproduced from [CHH00]); (b) the abundance of different charged states of C_{60} is compared with rates derived from S-matrix theory [JBF07].

where $r_0 = 6.69$. The functions $h(r, q)$ and $g(r, q)$ for the final charge state q are

$$h(r, q) = (q - 1)\left[0.143 + 0.00424r - 0.00063r^2\right] \tag{8.15}$$

and

$$g(r, q) = (q - 1)\left[-1/r + e^{-\alpha r}\sum_{i=0}^{4} A_i r^i\right] \tag{8.16}$$

with the parameters: $\alpha = 1.66194$, $A_0 = 484.16696$, $A_1 = -152.88756$, $A_2 = 12.47619$, $A_3 = -3.83926$, and $A_4 = 1.04143$.

8.1.4 Calculation of Ionisation Rates for C_{60}^{q+}

The ionisation rates for C_{60}^{q+} can be calculated in the SAE picture applying the S-matrix

theory [JBF07]. This theory provides quantitative estimations of transition probabilities in complex atoms, molecules, and clusters interacting with strong laser fields [JBF04]. Here the lowest order S-matrix theory, namely, the well known "Keldysh-Faisal-Reiss" (KFR) model [Rei80] is utilised to calculate total ionisation rates of C_{60} as a function of laser pulse duration.The total ion yield for the individual charge states is determined by summing over the contributions from all points in the laser focus. The comparison of the theoretical results with experimental data is shown in Fig. 8.3a. The calculated data are normalised to the maximum signal of C_{60}^{+}. Both experimental and theoretical data are plotted in Fig. 8.3b. The experimental ion yields of different charge states are scaled by the detection efficiency of the microchannel plates which depends on the impinging energy of C_{60}^{q+}.

The experimental data show the general trend of increasing abundance of multiply charged ions with increasing pulse duration. This trend is in a qualitative agreement with the theoretical modelling. Especially, good agreement is observed in the short pulse limit, where energy redistribution processes such as electron-electron scattering and coupling to the vibrational degrees of freedom, which are not included in the S-matrix theory, play a minor role. It indicates that the SAE assumption may be an appropriate model for the description of photoinduced processes in the limit of ultrashort laser pulses.

8.2 Pulse Duration Dependent Study

8.2.1 Experimental Observations

Here the experimental results for C_{60} photoionisation obtained in an intensity range between $3 \times 10^{13}\,\mathrm{W/cm^2}$ and $4 \times 10^{14}\,\mathrm{W/cm^2}$ with different laser pulse durations are presented. A detailed analysis of the experimentally determined ion yields measured as a function of laser intensity provides important information about photoinduced processes such as ionisation.

First, experiments with laser pulses centred at $765\,\mathrm{nm}$ at a pulse duration of $9\,\mathrm{fs}$ are discussed. Fig. 8.4a-e illustrates the characteristic dependence of charge states and the fragment mass distribution on laser intensity. At highest intensity of $3.7 \times 10^{14}\,\mathrm{W/cm^2}$ one observes charge states of C_{60}^{q+} up to $q = 5$, as well as a significant amount of multiply charged, fullerene-like fragments which have lost up to 8 units of C_2 as shown by the enlarged inset in Fig. 8.4a

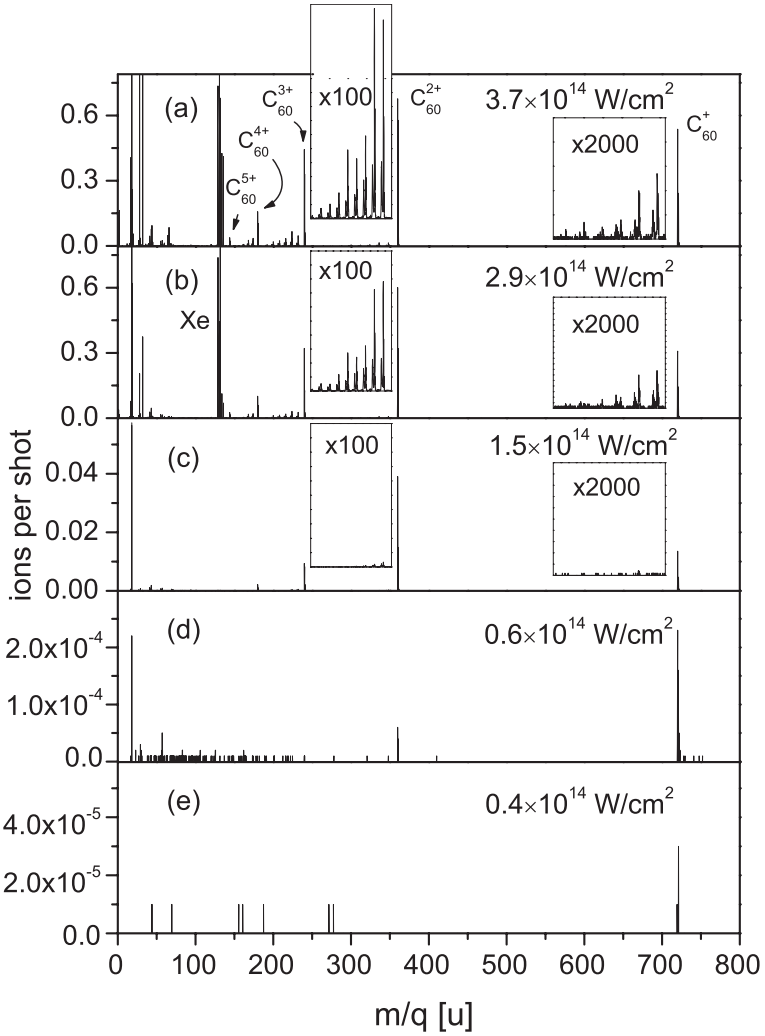

Figure 8.4: Mass spectra obtained from photoionisation of C_{60} with 9 fs laser pulses centred at 765 nm. The laser intensity decreases from 3.7×10^{14} W/cm^2 (a) to 4×10^{13} W/cm^2 (e).

(fragmentation of C_{60} is discussed in Chapter 9). With decreasing intensity the formation of ions decreases, especially so for the highest charge states of C_{60}. Finally, at 4×10^{13} W/cm^2 only C_{60}^+ is noticeable in the mass spectrum (Fig. 8.4e). For comparison a set of mass spectra is measured as a function of intensity for laser pulses with a duration of 27 fs centred at 797 nm.

Fig. 8.5a-b compare the ion yields for several final charge states of C_{60}^{q+} as a function of the laser intensity recorded with 27 fs and 9 fs pulses, respectively. The standard log-log plot is used to illustrate the power law (Eq. (8.1)) at intensities below saturation. The experimental data exhibit the characteristic saturation behaviour at high intensities for all charge states.

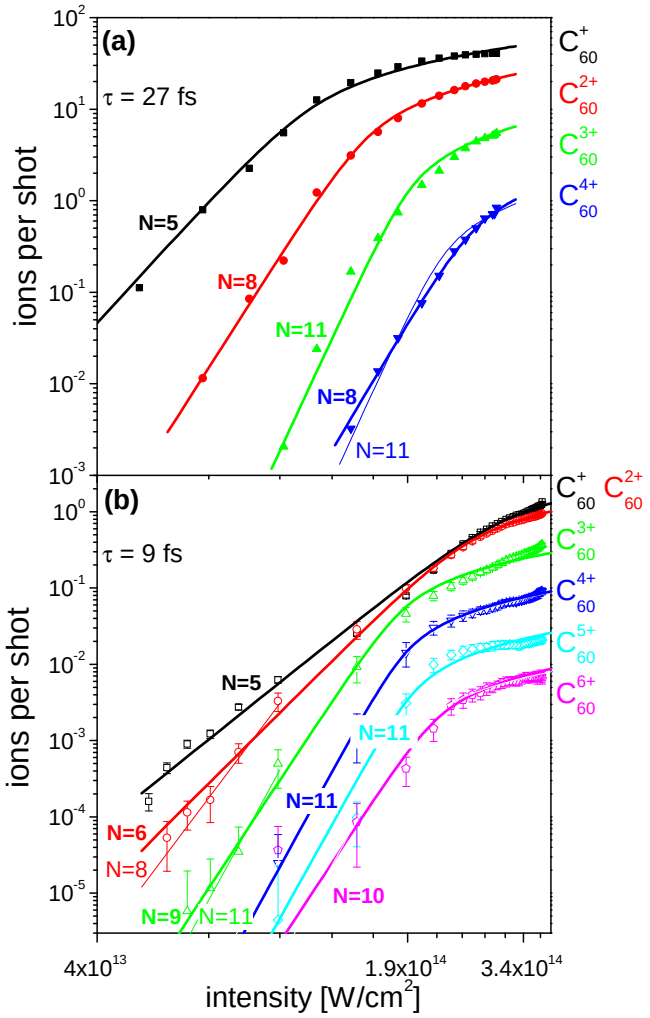

Figure 8.5: Experimental yields of C_{60}^{q+} ions measured as a function of intensity (symbols) and their fits (lines): (a) laser pulse duration is 27 fs; (b) laser pulse duration is 9 fs.

It is determined by the absolute magnitude of the MPI cross-section and the experimental geometry.

To extract values for the saturation intensity I_{sat} and the order (slope) N of the MPI at low intensities the data are fitted according to Eq. (8.10). The slopes obtained for the C_{60}^{q+} ion yield at low intensities (full lines in Fig. 8.5) for $q = 1, 2$, and 3 are $N = 5, 8$, and 11, respectively. For higher charge states the slopes remain essentially constant at $N = 10 \pm 2$. However, the statistics of the 9 fs experimental data does not allow one to make a fit with one unique slope for $q = 2$ and 3 over the whole intensity range (as indicated by the dashed lines in Fig. 8.5). For strictly stepwise MPI processes: $C_{60} \longrightarrow C_{60}^{+} \longrightarrow C_{60}^{2+} \longrightarrow C_{60}^{3+} \longrightarrow \ldots$

one would expect $N = 5, 8$, and 11 for $q = 1, 2$, and 3, respectively, and even higher values of N for larger charge states. In the SAE picture, N is the number of photons required to remove subsequently an additional electron after saturation of the precursor charge state. The remarkable fact is that the slopes derived meet the expectations only for $q = 1, 2$, and 3. But a stepwise MPI model does not explain constant or even falling values of N for higher charge states. Even more interesting is the observation that the slopes for $q = 2$ and 3 appear to reflect the number of photons one would need for ionisation $C_{60}^{(q-1)+} \longrightarrow C_{60}^{q+}$ in an intensity range, where the respective precursor is far from being saturated.

These observations clearly indicate the limitations of the SAE picture with sequential ionisation for such complex systems as C_{60} fullerenes. This may be due to the resonant pre-excitation to "doorway" state [LSS07], and/or to high lying electronic states close to ionisation threshold, possibly the Rydberg states [BLH05], and/or even due to collective excitation which will be discussed in the following. The theoretical calculations predict multielectron excitation even at intensities far below the presently observed saturation values [TNE01, ZSG03, ZGe04]. Consequently, many electrons are excited prior the ionisation and can possibly support simultaneous multielectron ejection.

The largest slope ($N = 11$) observed in the present experiment corresponds to a total photon energy of $17.8\,\text{eV}$ with laser pulses of $9\,\text{fs}$ duration at $765\,\text{nm}$. This energy is enough to excite the first maximum of the σ-part of the C_{60} giant plasmon resonance (see Sec. 2.1) [HSV92]. Fig. 2.3 illustrates this energetics for the single photon ion yield. According to this picture, even for 8 photons there is substantial oscillator strength in the ionisation continuum. Therefore, if the plasmon resonance is sufficiently excited, any further excitation is very efficient due to the absorption of photons by the hot electron-hole plasma. Thus, the transition saturates and no further increase in the slope is observed, while at the same time multiple ionisation can occur. Indeed, it might explain both the observed slopes $N = 8$ and 11 for $q = 2$ and 3, respectively, at low intensities and the absence of slopes increasing for higher charge states. After the excitation of the giant plasmon the system is bound to undergo non-adiabatic multielectron dynamics (NMED) [MRS04]. Then, sequential or non-sequential non-adiabatic excitation is driven by the strong laser field which mixes the dense manyfold of electronic states in this energy range.

8.2.2 Sequential Ionisation

To further critically interrogate the usually assumed concept of sequential ionisation, the coupled differential equations for single and double ionisation of C_{60} are treated for such a stepwise process

$$C_{60} + Nh\nu \longrightarrow C_{60}^{+} + e^{-}, \quad E_{IP} = 7.6 \text{ eV} \tag{8.17}$$

and

$$C_{60}^{+} + Mh\nu \longrightarrow C_{60}^{2+} + e^{-}, \quad E_{IP} = 11.4 \text{ eV} \quad . \tag{8.18}$$

From Eq. (8.3) the reduction of the initial (neutral) C_{60} density n_0 during the laser excitation is given by

$$\frac{dn_0(r,t)}{dt} = -n_0(r,t)\gamma_N I^N(r,t) \quad . \tag{8.19}$$

The densities of singly and doubly charged species (n_1 and n_2, respectively) are obtained from

$$\frac{dn_1(r,t)}{dt} = n_0(r,t)\gamma_N I^N(r,t) - n_1(r,t)\gamma_M I^M(r,t) \tag{8.20}$$

and

$$n_2 = n_0(r,0) - n_0(r,t) - n_1(r,t) \quad . \tag{8.21}$$

For a given peak pulse intensity I_0 the coupled rate Eqs. 8.19-8.21 have been solved numerically by integrating over the Gaussian beam profile and the cylindrical interaction volume using the experimental parameters reported in Chapter 6. The results plotted on a log-log scale are shown in Fig. 8.6. The calculation was performed for $800\,$nm laser pulses with a duration of $27\,$fs, setting the power laws according to the ionisation potentials ($7.6\,$eV and $11.4\,$eV) to $N = 5$ and $M = 8$ for stepwise ionisation. Two different sets of saturation intensities were used for these model calculations: $I_{sat}(C_{60}^{+}) = 1 \times 10^{13}\,\text{W/cm}^2$, $I_{sat}(C_{60}^{2+}) = 1 \times 10^{14}\,\text{W/cm}^2$ as shown in Fig. 8.6a and alternatively $I_{sat}(C_{60}^{+}) = 1.00 \times 10^{14}\,\text{W/cm}^2$, $I_{sat}(C_{60}^{2+}) = 1.39 \times 10^{14}\,\text{W/cm}^2$ as shown in Fig. 8.6b (the latter set of I_{sat} represents the experimentally derived values reported later).

The C_{60}^{+} ion yield shows a reasonable behaviour for intensities below saturation with a slope of $N = 5$ in agreement with the corresponding power law. However, the yield of C_{60}^{2+} exhibits the expected slope $M = 8$ expected for sequential ionisation only for intensities above the saturation of C_{60}^{+}. Hence, the saturation intensity for C_{60}^{+} had to be chosen a factor of 10 below that for C_{60}^{2+} as illustrated in Fig. 8.6a. On the other hand, according to the rate

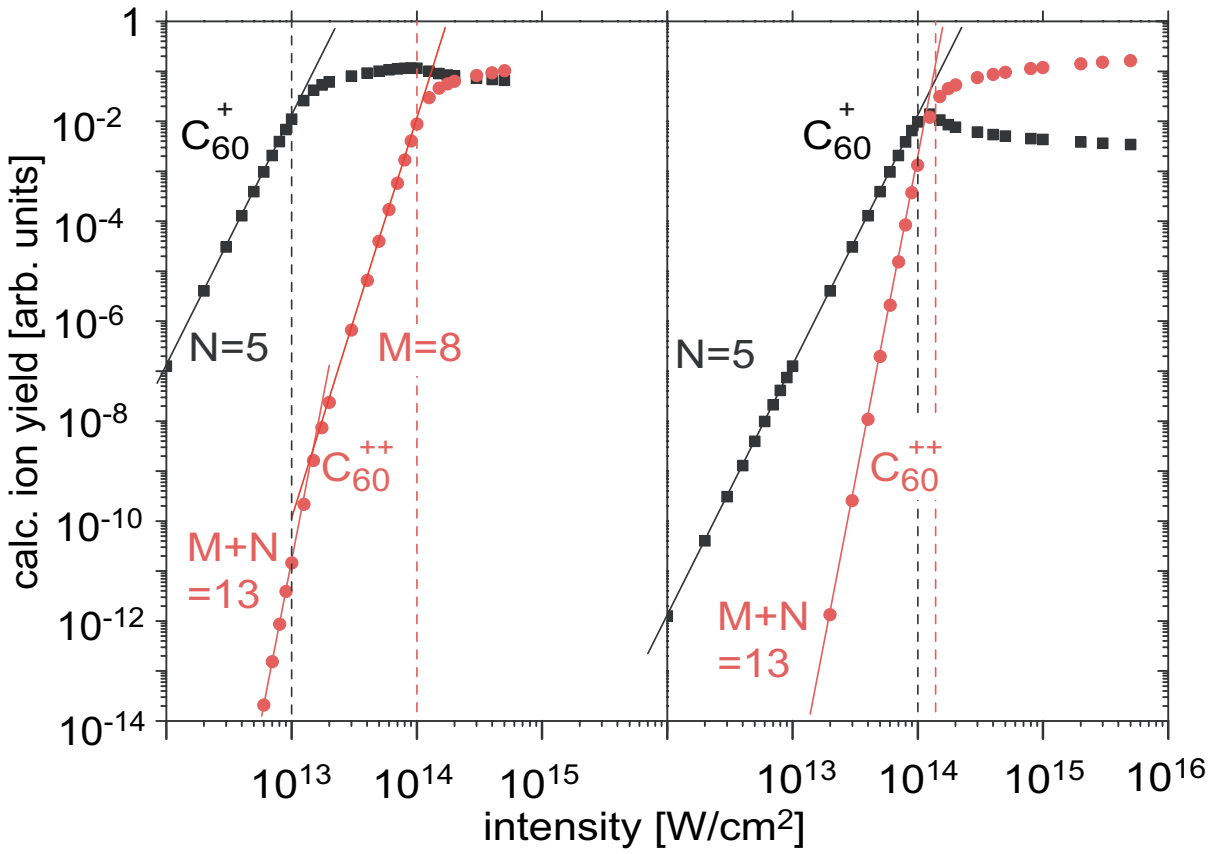

Figure 8.6: Yields of C_{60}^{+} and C_{60}^{2+} calculated by solving the coupled differential equations assuming two different sets of saturation intensities for C_{60}^{+} and C_{60}^{2+}: (a) 1×10^{13} W/cm^2 and 1×10^{14} W/cm^2, respectively; (b) 1.00×10^{14} W/cm^2 and 1.39×10^{14} W/cm^2, respectively.

equation model using the measured values of the saturation intensities, the yield of C_{60}^{2+} follows a power law with a slope of $N + M = 13$ and overshoots the C_{60}^{+} yield at higher intensities by more than one order of magnitude (Fig. 8.6b).

8.2.3 Saturation Intensities

The saturation intensities derived from the fits of the experimental data presented in Fig. 8.5a-b are plotted as a function of the final charge state q in Fig. 8.7. The values of saturation intensities obtained with 9 fs and 27 fs laser pulses are indicated by magenta squares and red circles, respectively. For comparison saturation intensities measured with 70 fs pulses at 1800 nm (brown triangles) [BCR03] and with 45 fs pulses at 395 nm (blue diamonds) [THD00] are also shown. The brown dashed line in Fig. 8.7 shows the theoretical prediction based on the classical over the barrier ionisation mechanism for the conducting sphere model of

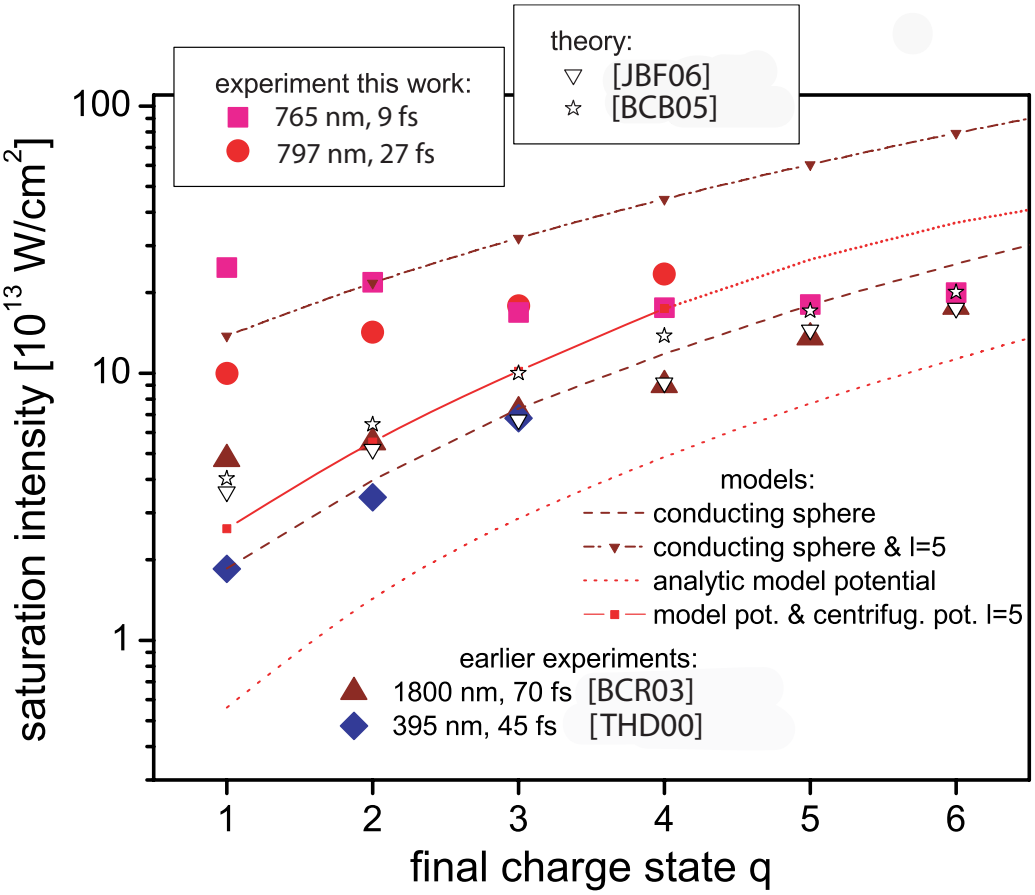

Figure 8.7: Saturation intensities for C_{60}^{q+} ions as a function of the final charge state q. Experimental data obtained with 70 fs pulses at 1800 nm (triangles) and with 45 fs pulses at 395 nm (diamonds) are taken from [BCR03] and [THD00], respectively. The present data obtained with 765 nm, 9 fs and 797 nm, 27 fs are indicated by squares and circles, respectively. The experimental data are compared to theoretical models: over the barrier ionisation using the conducting sphere model [BCR03] and the model potential (Eq. (8.22)) including polarisation screening with and without centrifugal barrier as well as theory from [BCB05] and [JBF06].

C_{60} with polarisation screening for a wavelength of 1800 nm from [BCR03]. In contrast to the original publication the ionisation potentials described by Eq. (8.13) are used here. This model describes the experimental data for the higher charge states ($q = 3 - 6$) quite well, but large deviations between theory and experiment are observed for $q = 1$ and 2. Saturation intensities from the same ionisation model, but using a more realistic potential described by Eq. (8.14), are also given. In this case the overall interaction potential $U(r)$ including the laser field, the field induced dipole, and the centrifugal barrier for an ejected electron in a spherical

approximation is given by

$$U(r) = U(r,q) + E_0\left(r\cos\theta - \alpha/r^2\right) + l(l+1)/\left(2r^2\right) \quad , \tag{8.22}$$

where $U(r,q)$ is the jellium type potential described by Eq. (8.14), E_0 is the laser field amplitude, α is the polarisability of C_{60}, and l is the angular momentum. The red dotted line in Fig. 8.7 shows the result using this potential, but without the centrifugal barrier. The experimental saturation intensities are underestimated for all charge states by nearly one order of magnitude in this model. Taking into account the centrifugal barrier with the angular momentum $l = 5$, which corresponds to the angular momentum of the h_u ground state electrons, gives results (red lines with dots) which are very similar to the theoretical values obtained with the above described conducting sphere model. While on the other hand, the conducting sphere model with the centrifugal barrier gives the saturation intensities (brown line with dots) which are much higher than the experimental values. Based on these results, one can concludes that the centrifugal barrier is important for understanding the high saturation intensities for C_{60}^{g+} in terms of the above barrier model. This conclusion is supported by recent theoretical work [BCB05], where it was found that the width and the shape of the momentum distribution in complex systems demonstrate strong deviations from conventional tunnelling ionisation theories.

However, important experimental parameters such as laser pulse duration and central wavelength do not enter into the above barrier model at all. Therefore, to explain the observed dependencies of the saturation intensities on laser parameters a more detailed description is required. A key result is that the saturation intensities for low charge states depend significantly on the laser wavelength in direct contrast to the quasi-static classical tunnelling and over the barrier ADK theory. A special case is the ionisation with 395 nm laser pulses which is very likely affected by the t_{1g} resonance in the neutral C_{60}. This can explain the significantly lower experimental saturation values. In this context, it is also interesting to compare the saturation intensities measured with 9 fs and 27 fs laser pulses. For the lowest charge state ($q = 1$) the 9 fs value is about 2.5 times higher than the result with 27 fs. While the 27 fs data show a weak but monotonic increase of the saturation intensity as a function of the charge state, the 9 fs data even slightly decrease with the charge state. This observation can not be explained by any simple above barrier stepwise picture. According to Eq. (8.8) on can compare equivalent intensities I_1 and I_2 for different durations τ_1 and τ_2 of laser pulses with similar

shapes using the following expression

$$\frac{I_1}{I_2} = \left(\frac{\tau_2}{\tau_1}\right)^{1/N} \quad . \tag{8.23}$$

This formula may be utilised to compare saturation intensities measured with different laser pulse durations. Unfortunately, the difference between the saturation intensities obtained with $9\,$fs and $27\,$fs pulses can not be simply expressed by Eq. (8.23) indicating complex nature of C_{60} ionisation mechanisms.

8.3 Polarisation Dependent Study

8.3.1 Photoion Spectroscopy

Investigations of effects induced by the laser light ellipticity play a significant role in studying ionisation mechanisms. The influence of the light ellipticity on single and double ionisation and high order harmonic generation (HHG) is quite good known for atoms and small molecules [FKM02, SLW03]. In this case a reduction of ion and HHG yields is attributed to the recolliding electron being driven away from its origin by circularly as opposed to linearly polarised light. At the same time, apart from [BCR04] and one pioneering study at particularly high intensities [RKM03] only little is known about the role of ellipticity in the energy deposition process during the interaction of intense laser pulses with complex molecular systems. To get additional information about C_{60} ionisation mechanisms and, especially, about the influence of electrons recollision on ionisation, the effect of the laser light ellipticity on C_{60} ionisation was investigated in details. Key questions are whether here recollision effects can be identified and/or whether a particular signature of the doorway state can be found.

Resent studies at longer wavelength ($1500\,$nm) have demonstrated the importance of the recollision process in fragmentation from higher charged states of C_{60}^{q+} ($q = 3, 4$) [BCR04]. With long wavelength one purely goes into the tunnelling ionisation regime at lower laser intensity. Indeed, the Keldysh parameter γ is ≈ 0.2 for the experimental conditions described in [BCR04], implying a ponderomotive potential $U_P = 95\,$eV which is proportional to the square of the laser wavelength (Sec. 3.1). Hence, energies of the rescattered electrons of up to $3.17U_P = 300\,$eV are encountered in this process that can safely be described by a

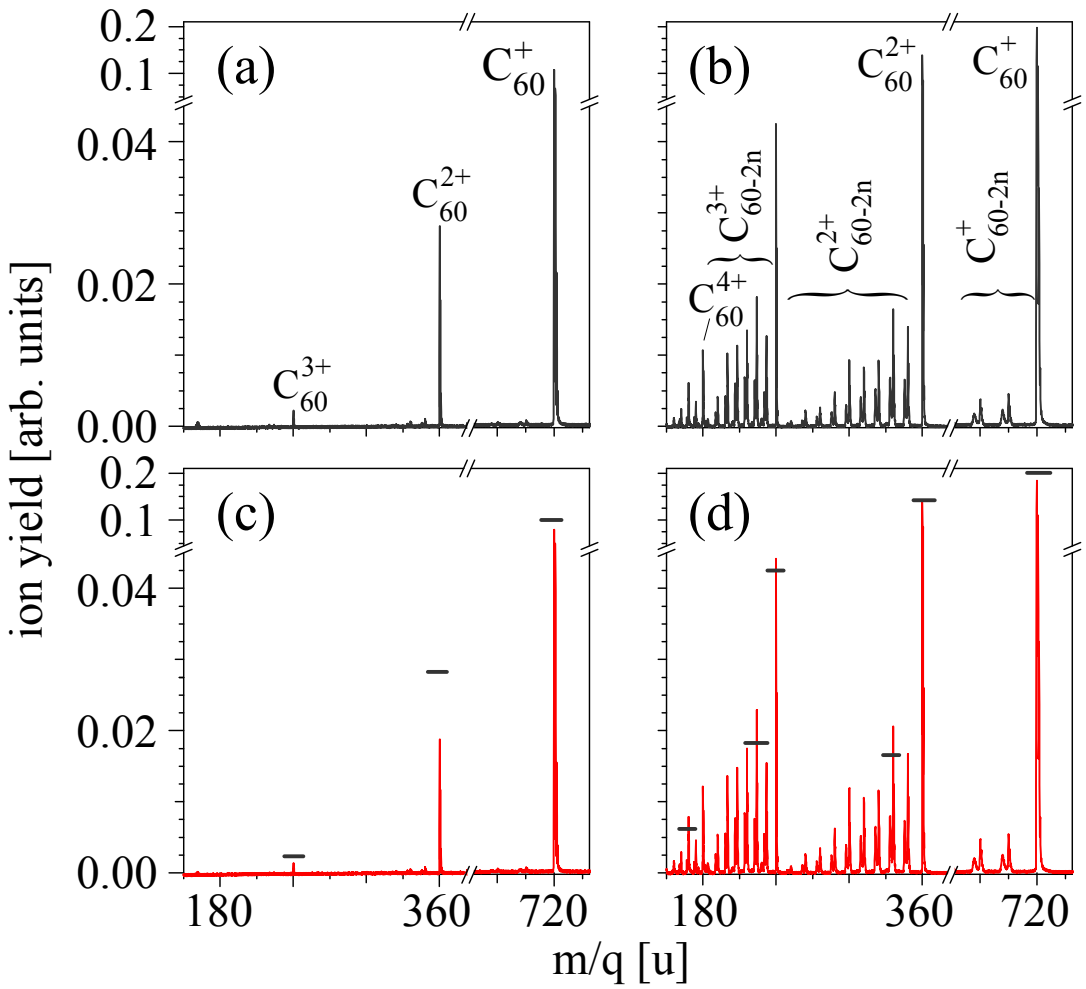

Figure 8.8: (a), (b) Mass spectra of C_{60} obtained with linearly polarised laser radiation of 27 fs pulse duration centred at 797 nm with intensity of 9×10^{13} W/cm^2 and 4.1×10^{14} W/cm^2, respectively. (c), (d) Mass spectra obtained with circularly polarised laser radiation with the same intensities as in (a) and (b), respectively. The small horizontal lines in (c) and (d) indicate the peak maxima in (a) and (b), respectively.

single active electron (SAE) [NKS07]. For shorter wavelengths, which are used in this work, U_p is typically much smaller and the ionisation process is more complex due to competition between multiphoton ionisation, tunnelling, excitation of intermediate electronic states and non-adiabatic multielectron dynamics (NMED).

Generally, the ionisation rate may be affected by the polarisation of the laser field for various reasons: (i) maximum field amplitude for linear polarisation is $\sqrt{2}$ times the constant circularly polarised field for any given average intensity; (ii) if multiphoton absorption dominates, special angular momentum selection rules may also be significant; (iii) the efficiency of the recollision is determined by the trajectory of the electron being driven away from its origin by circularly

as opposed to linearly polarised light. More efficient ionisation with circular polarised laser radiation at higher intensities was theoretically predicted for H atoms in *ab initio* quantum mechanical calculations [PLK97]. Recently similar results have been experimentally observed for ionisation of NO with 800 nm laser pulses [GGi01] and qualitatively described with ADK model [ADK86]. However, the ADK theory may not give an accurate description of ionisation of complex molecules.

Fig. 8.8 shows mass spectra recorded with 27 fs pulses centred at 797 nm and intensity of 9×10^{13} W/cm^2 for linear (Fig. 8.8a) and circular (Fig. 8.8c) light polarisation as well as with intensity of 4.1×10^{14} W/cm^2 for linear (Fig. 8.8b) and circular (Fig. 8.8d) polarisation. Fig. 8.8a-b reproduce the well known C_{60} mass spectra obtained with short linearly polarised laser pulses. At intensities below 1×10^{14} W/cm^2 intact C_{60}^{q+} ions are observed with charge states $q \leq 3$, while for higher intensities fullerene-like fragments (C_{60-2n}^{q+}) appear in the mass spectrum especially for $q \geq 2$. At first glance, the mass spectra shown in Fig. 8.8c-d taken with circularly polarised laser pulses look very similar. However, a closer inspection shows small but significant differences as indicated by the small horizontal bars on top of the mass peaks in Fig. 8.8c-d, representing the respective signals in Fig. 8.8a-b, respectively. At lower intensities the ion signals decrease by approximately 25%, when changing the polarisation from linear to circular. On the other hand, by comparing Fig. 8.8b and Fig. 8.8d one finds that for high intensities the ion signals of the fullerene-like fragments even increase up to 20%, when circularly polarised light is used, while the ion signals of the intact C_{60}^{q+} ions are almost unchanged. These first qualitative inspections already hint at interesting effects of the laser intensity and ellipticity on the excitation and ionisation process in complex systems.

Before discussing the C_{60} results the Xe^+ ion yield, which can be viewed as a supposedly simple test case, will be considered. The overall dependence of the Xe^+ ion yield on laser pulse intensity (linearly polarised) is well known from the literature [LTC98]. With an ionisation potential of 12.13 eV at least 8 photons are needed to generate the lowest ionic state $Xe^+(^2P_{3/2})$, but a number of intermediate resonances obscure the expected power law (see Sec. 3.2) somewhat. Thus, the log-log plot of ion yield as a function of intensity shows a slope of 8 only for intensities below 10^{13} W/cm^2, while between 3×10^{13} W/cm^2 and saturation intensity of $I_s \simeq 10^{14}$ W/cm^2 a slope of 5 is observed, giving evidence for an effective 5 photon process.

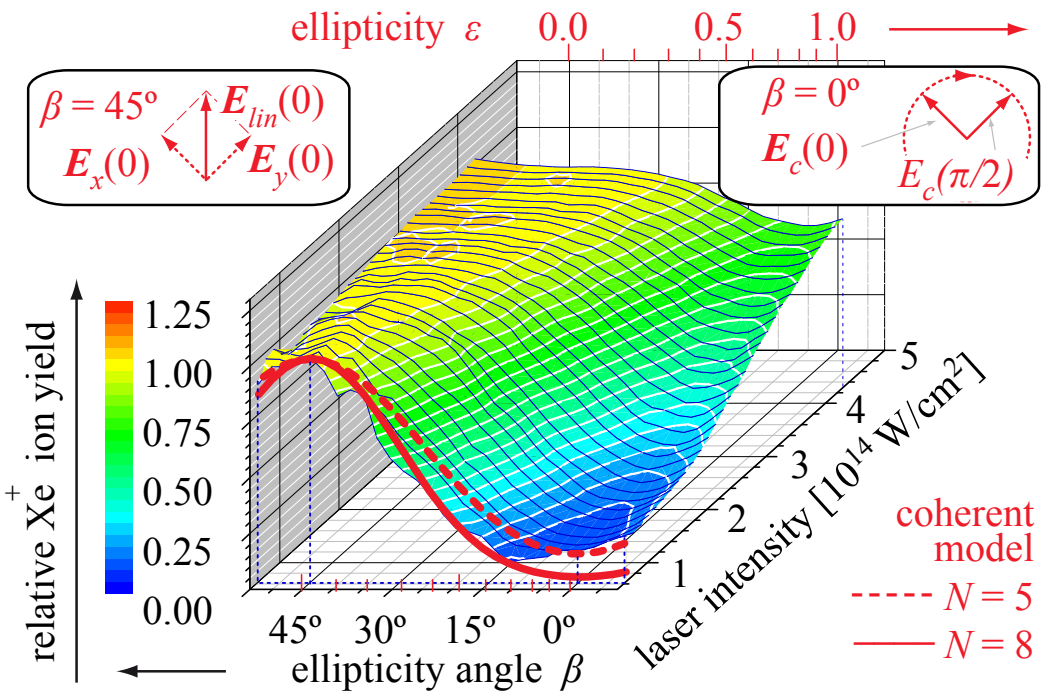

Figure 8.9: Integrated yield of Xe^+ measured at 797 nm normalised to the yield with linear light polarisation plotted as a function of ellipticity angle β and laser intensity. The polarisation changes from linear ($\beta = 45°$) to circular ($\beta = 0°$). The full and dashed red lines at $I = 0.65 \times 10^{14}$ W/cm^2 correspond to coherent excitation in an 8- and 5-photon processes, respectively. Two inserts illustrate that the maximum field amplitude for linear polarisation is $\sqrt{2}$ times the constant circularly polarised field for any given average intensity.

Ellipticity dependence of the ion yield as a function of the laser intensity can be considered using the "classical averaging" model described in Sec. 5.5. Eq. (5.51) predicts a drop of the effective multiphoton cross-section between linear and circular polarisation as a direct consequence of the fact that the electric field vector for circularly polarised light is constant but only $1/\sqrt{2}$ of that for the maximum of linearly polarised light.

Fig. 8.9 shows a 3D plot of the integrated Xe^+ yield as a function of both, laser intensity and ellipticity angle β which is related to the often used ellipticity ε according to Eq. (5.45). To compensate for the strong intensity dependence of the ion yield the present experimental data are normalised to their values for linear polarisation. When the polarisation changes from linear to circular, a dramatic drop of the signal is observed at all intensities, but most significantly at the lower intensities. While for higher intensities, where the saturation for the ion signals has been reached, some reduction of this trend is recognised. The dashed red

line in Fig. 8.9 represents the results of the classical averaging model described by Eq. (5.51) with $N = 5$ at an intensity of $I = 0.65 \times 10^{14}\,\mathrm{W/cm^2}$ which has been chosen significantly below the saturation intensity for Xe^+ ion formation. This theoretical model ($N = 5$) roughly reflects the experimentally observed trend. An even better fit is found, if $N = 8$ is assumed, as shown by the full red line in Fig. 8.9. Interestingly, ionisation of Xe requires indeed at least $\simeq 8\hbar\omega_0$ ($\lambda = 797\,\mathrm{nm}$). There is no conclusive explanation for this finding. However, the slope I^5 intensity dependence is usually attributed to "population trapping" in high lying states [TCC96] which is obviously not reflected in the β-dependence. In that sense, the polarisation dependent studies probe the order of the photon absorption process in a much more sensitive manner than ion yield measurements.

Now the main subject will be considered. The measured ion yield for C_{60}^+ and C_{60}^{3+} is shown in Fig. 8.10. In both cases a small, but very clear reduction of the signal for circularly polarised light is seen at low intensities ($< 1 \times 10^{14}\,\mathrm{W/cm^2}$). Here the ponderomotive potential is only $\simeq 5\,\mathrm{eV}$ and recolliding electrons can not play a significant role. However, a nearly perfect match of the observed β-dependence (low intensity) is found with an average intensity distribution $\langle I^2(t,\beta)\rangle$ for a coherent two photon process as indicated by the full red line in Fig. 8.10. This remarkable result gives clear evidence to the importance of the t_{1g} doorway state which can be populated by such a coherent two photon excitation. At higher intensities the β-dependence decreases and the ion yields become almost independent of ellipticity. This can be attributed to saturation of the ionisation process.

For the current laser parameters the ion yields of C_{60}^+ and C_{60}^{3+} are $\propto I^N$ with $N = 5$ and 11, respectively. In case of C_{60}^+ and C_{60}^{3+} the corresponding dependencies (5 and 11) are not observed as a function of ellipticity (in contrast to the Xe^+ case). This gives strong evidence for genuine multielectron processes dominating the ionisation and energy deposition in C_{60}: once the doorway state is reached, many electrons can absorb energy through transitions in a quasi-continuum of states which in fact explains the high number of photons absorbed. If more or less loosely coupled chromophore electrons each absorbs one photon, one expects no polarisation dependence. For a process which requires an energy equivalent of at least 5 photons (such as C_{60}^+ formation), the intensity dependence will nevertheless be $\propto I^5$ since 5 photons must be absorbed during the interaction with the laser pulse. These processes are, however, no longer coherent since several electrons are involved independently. The

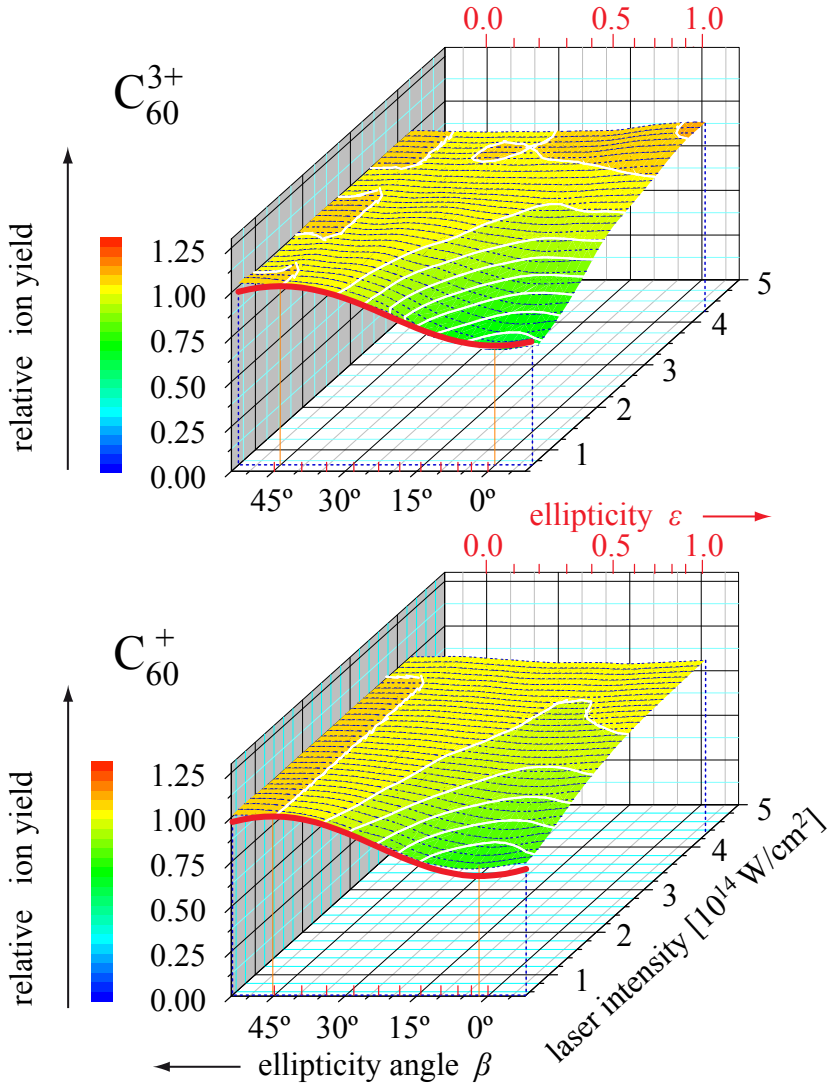

Figure 8.10: Integrated yield of C_{60}^{+} and C_{60}^{3+} measured at 797 nm normalised to the yield with linear light polarisation plotted as a function of ellipticity angle and laser intensity. The full red lines correspond to coherent excitation in a 2-photon process.

corresponding statements also hold for higher charge states.

As a crucial test the ellipticity dependence of the C_{60}^{q+} signals at $\lambda = 399$ nm for laser intensities between 0.2×10^{13} W/cm^2 and 4.0×10^{13} W/cm^2 was measured. The corresponding plots presented in Fig. 8.11 are absolutely flat to within 1%, while the ion yields at this wavelength were found to be $\propto I^3$ and $\propto I^6$ for C_{60}^{+} and C_{60}^{3+}, respectively [THD00]. This strongly confirms the key role of the doorway state, being excited by absorption of a single 399 nm photon so that its population depends only on I_0 and not on β. Again, subsequent photons are deposited via different chromophore electrons of which each absorbs one photon.

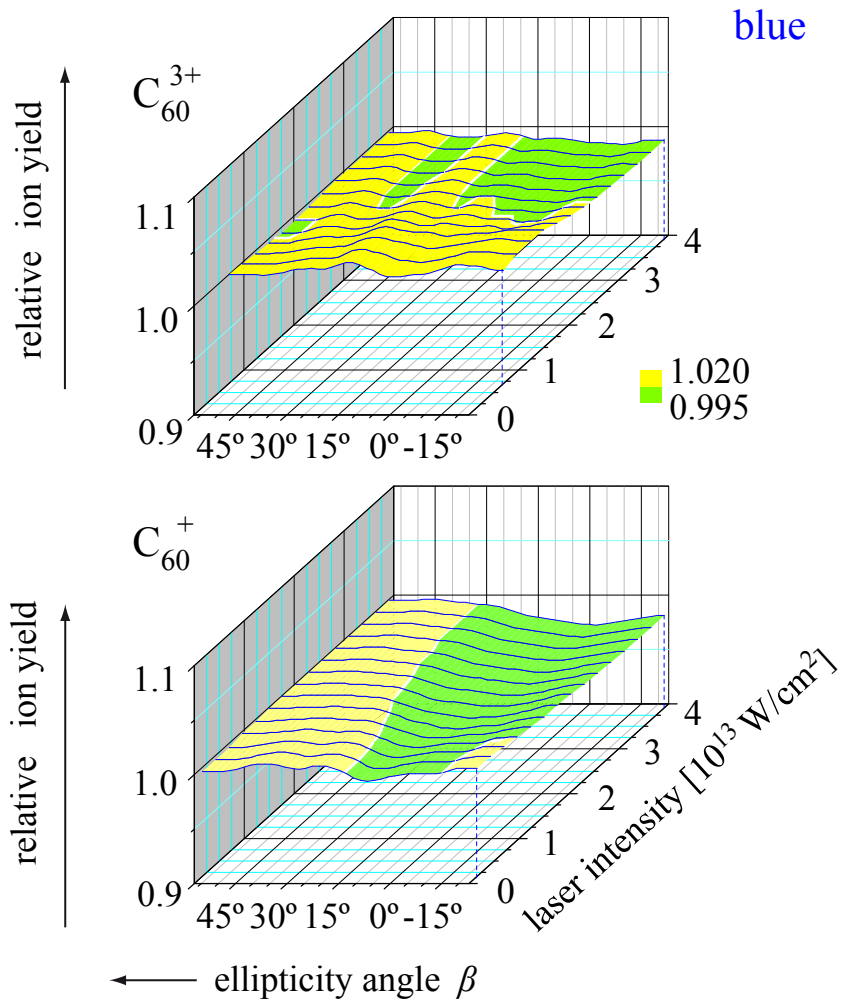

Figure 8.11: Integrated yield of C_{60}^{+} and C_{60}^{3+} normalised to the yield with linear light polarisation plotted as a function of ellipticity angle and laser intensity after interaction of C_{60} with 399 nm laser pulses. Here complete independence on ellipticity at all intensities is found, in contrast to corresponding measurements with 797 nm pulses.

The behaviour of the fullerene-like fragments C_{60-2n}^{q+} is even more surprising. Fig. 8.12 shows the singly and triply charged ion yield summed over all fragments $n \geq 1$. For the lower intensities again the coherent two photon signature $\langle I^2(t,\beta)\rangle$ (at least for C_{60-2n}^{3+}, while C_{60-2n}^{+} fragments are very weak and the noisy signal does not allow one to make a clear conclusion) can be recognised. However, at higher intensities a significant enhancement of the fragment signal is observed with circularly polarised light. At first sight, this appears to be against all common wisdom: typically the signals decrease with circularly polarised light. One potential explanation could be complicated multiphoton processes with absorption and induced emission steps leading to constructive interference. In view of the fact that at high

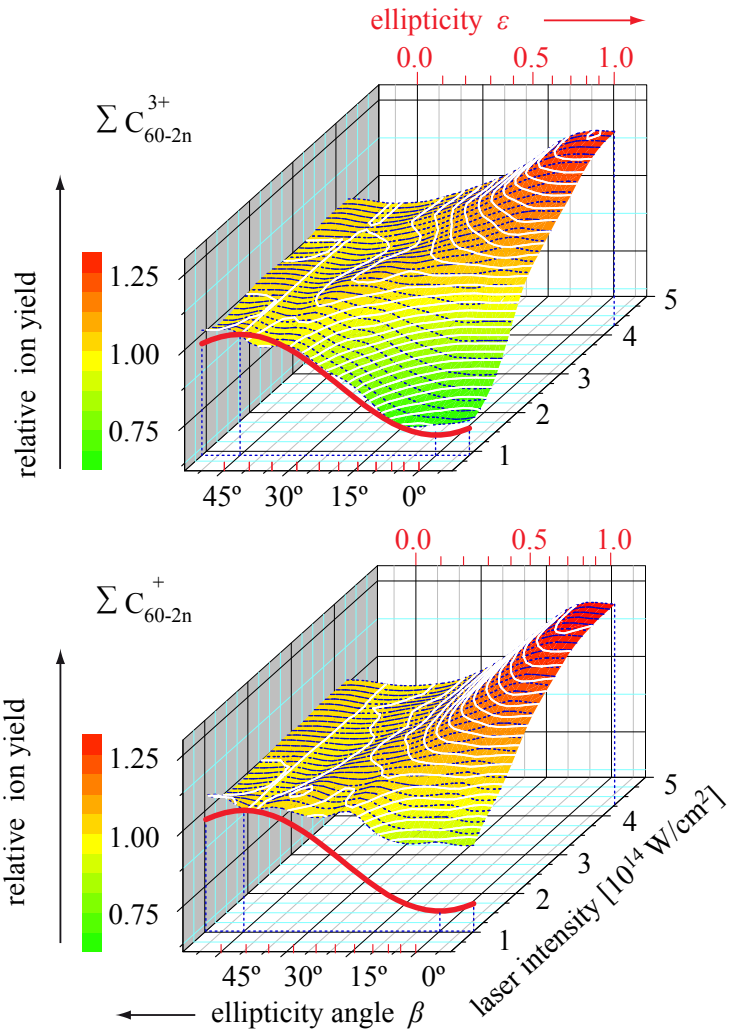

Figure 8.12: Integrated yield (enlarged scale) of fragments ΣC^{+}_{60-2n} and ΣC^{3+}_{60-2n} measured at 797 nm normalised to the yield with linear light polarisation plotted as a function of ellipticity angle and laser intensity. The full red lines correspond to coherent excitation in a 2-photon process.

intensities a multitude of intermediate states could play a role, in particular the intense giant resonance between the first ionisation threshold and about 35 eV. This is just pure speculation and the question is, of course, why this should be specific to generate fragments rather than higher charge states.

However, taking into account the potential influence of rescattered electrons, alternative explanations can also be discussed. Even in the classical trajectory picture one might imagine loops of recolliding electrons in a circularly polarised electric field (especially so, if the electrons ejected have initial kinetic energy [SGP08]). Rescattering for extended atomic systems has recently also been discussed in the context of Xe and Ar cluster ionisation [SRo08]. In contrast

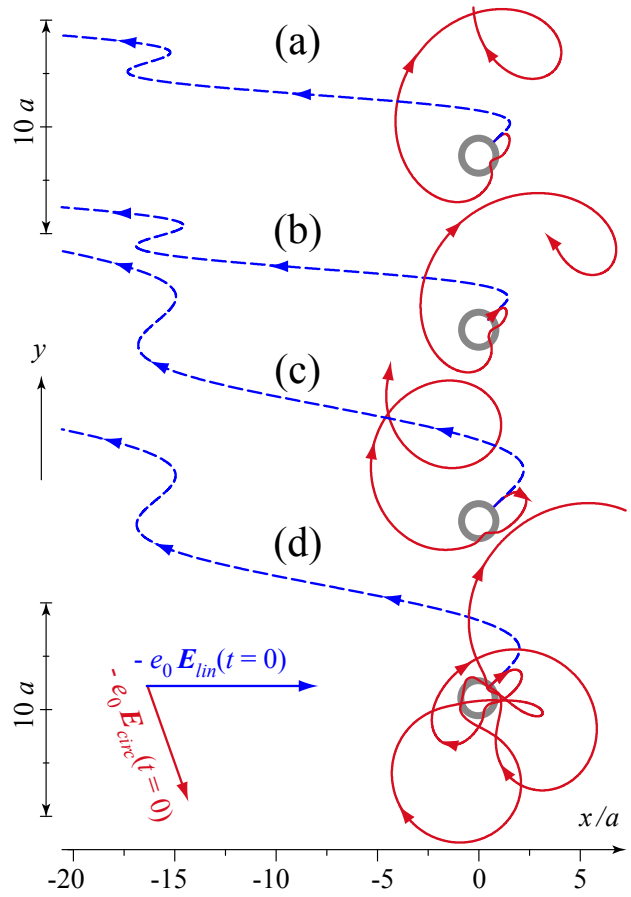

Figure 8.13: Examples of classical electron trajectories in the combined field of C_{60}^{+} and linearly (dashed blue lines) or circularly (full red lines) polarised light. $I = 4.3\times10^{14}$ W/cm^2, 797 nm , electron initial kinetic energy is 1 eV (a,b) or 10 eV (c,d), starting point of the trajectory is $0.65a$ (b,d) or $1.00a$ (a,c), $\Phi = \pi/4$, $\Theta = \pi/2$ (for details see text). The initial field phase at $t = 0$ is $\varphi = 162°$ in all cases shown, implying that the force on the electron at $t = 0$ points into the direction of $-72°$ for circularly and into the direction of $0°$ for linearly polarised light as indicated by the vectors. The thick full gray circles indicate the C_{60} shell radius $0.65a \ldots 1.00a$.

to single atoms, in C_{60} the photoionised (or tunnelling) electrons emerge from a sphere with radius $\geq a \simeq 8.12$ a.u., the C_{60} shell radius [DDE96]. They may even be ejected with relatively high initial kinetic energy due to strong field absorption of many photons. If e.g. the C_{60} plasmon resonance supports the photo absorption process in the continuum [SLS06], one expects initial kinetic energies of up to 30 eV. Assuming the electrons to be ejected radially this will lead most trajectories in a linearly polarised field to miss the C_{60} on return. In contrast, one may find a number of trajectories in a circularly polarised field which return, even several times, as exemplified in Fig. 8.13 for a few specific initial parameters.

Using classical mechanics to describe the electron motion $\mathbf{r}(t)$ one can write

$$\mathbf{r}''(t) = \frac{\mathbf{F}(r)}{m_e} - s(\rho)\frac{e_0\mathbf{E}(t)}{m_e} \quad , \tag{8.24}$$

where m_e is the electron mass, e_0 is the electron charge, $\mathbf{E}(t)$ is the electric field of the laser radiation, and $|\mathbf{F}(r)| = -e_0 dV(r)/dr$ is the force derived from a model potential by which the C_{60} core acts on the electron.

For the present classical trajectory studies a commonly used model potential $V(r)$ for the C_{60}^{q+} ions is employed [PNi93]. It is parameterised similarly to that given in Sec. 8.1. It describes C_{60}^{+} essentially as a potential well with outer and inner radius $a = 4.2916 \times 10^{-10}$ m and $b = 0.65a$, respectively, approaching asymptotically a Z/r Coulomb potential for $r \gg a$. For the present classical trajectory calculations the model potential in its most recent form [MCR08] is approximated by smoothing the very sharp (and physically unrealistic) edges over a width of $w = 0.15a$ using sigmoid functions, while the potential depth was adjusted for $Z = 1$ to $V_0 = 1.633$ so that the binding energy of the additional electron corresponds to the experimental values -7.56 eV. The model potential (in a.u.) is

$$V(r) = -\frac{q_a e^{\frac{a-r}{w_1}} + Z}{r}\frac{1}{1+e^{\frac{a-r}{w}}} - \left(V_0 + \frac{Z-1}{a+b}\right) \times \left(\frac{1}{1+e^{\frac{r-a}{w}}} + \frac{1}{1+e^{\frac{b-r}{w}}} - 1\right) - \\ - \frac{q_i e^{\frac{r-b}{w_1}} + q_0}{a}\frac{1}{1+e^{\frac{r-b}{w}}} \tag{8.25}$$

with $w_1 = 1.59$, $q_a = 4.5$, $q_i = 2.68$, and $q_0 = 0.73$.

The function $s(\rho)$ describes polarisation screening [BCR03] of the laser field outside the C_{60}^{q+} and in addition screening of the field inside so that it can not penetrate into the C_{60} core. A cutoff function, which serves this purpose sufficiently well, is used for simplicity

$$s(\rho) = \frac{1}{1+e^{\frac{1.5a-\rho}{0.4a}}} \tag{8.26}$$

with $\rho(t) = \sqrt{x^2(t)+y^2(t)}$ (assuming the electric field vector to lie in the xy-plane). Setting $|\mathbf{r}(t)| = \sqrt{x^2(t)+y^2(t)+z^2(t)}$ Eq. (8.24) can be rewritten as

$$\begin{aligned} x''(t) &= \frac{s(\rho)e_0}{m_e}E_0 \sin(\beta+\pi/4)\sin(\omega_0 t+\varphi) + \frac{x}{r}\frac{F(r)}{m_e} \\ y''(t) &= \frac{s(\rho)e_0}{m_e}E_0 \cos(\beta+\pi/4)\cos(\omega_0 t+\varphi) + \frac{y}{r}\frac{F(r)}{m_e} \\ z''(t) &= \frac{z}{r}\frac{F(r)}{m_e} \quad . \end{aligned} \tag{8.27}$$

E_0, ω_0, φ, and β are the electric field amplitude, frequency, phase, and ellipticity angle, respectively. Assuming the electron to be ejected radially with a total initial kinetic energy W_{in} from the C_{60} molecule at a position $\mathbf{r}(0) = \{r_0 \sin\Theta\cos\Phi; r_0 \sin\Theta\sin\Phi; r_0\cos\Theta\}$ the following initial conditions have to be implemented

$$\begin{aligned} x(0) &= r_0 \sin\Theta\cos\Phi \\ y(0) &= r_0 \sin\Theta\sin\Phi \\ z(0) &= r_0 \cos\Theta \\ x'(0) &= \sqrt{2T_{in}/m_e}\sin\Theta\cos\Phi \\ y'(0) &= \sqrt{2T_{in}/m_e}\sin\Theta\sin\Phi \\ z'(0) &= \sqrt{2T_{in}/m_e}\cos\Theta \end{aligned} \tag{8.28}$$

with

$$T_{in} = W_{in} + |V(r_0)| \quad . \tag{8.29}$$

To derive $r(t)$ as well as the electron kinetic energy $W(t)$ a set of the differential equations Eq. (8.27) with the initial conditions Eq. (8.28) is solved using *Mathematica*. The recollision on return occurs if the following condition is satisfied

$$r_{rec} \equiv |\mathbf{r}(t_{rec})| = r_0 \quad , \tag{8.30}$$

where t_{rec} ($t_{rec} > 0$) is the time when recollision happened. The kinetic energy of the recolliding electron is

$$W_{rec} = \frac{m_e\left(\mathbf{r}'(t_{rec})\right)^2}{2} - |V(r_{rec})| \quad . \tag{8.31}$$

Experimental observations together with the trajectory studies at long wavelength of 1500 nm documented that fragmentation is significantly amplified by recollision in linear polarised laser fields [BCR04]. In contrast, the present classical trajectory calculations for the wavelength of 800 nm demonstrate that electron trajectories in a circularly polarised field starting on the C_{60} radius a or at the inner shell radius $0.65a$ return significantly more often as illustrated in Fig. 8.13.

To quantitative investigate influence of the numerous parameters entering in Eq. (8.27) and Eq. (8.28) on the kinetic energy of the recolliding electrons statistical test using a Monte Carlo approach is performed. W_{rec} is calculated 100000 times starting with uniform random

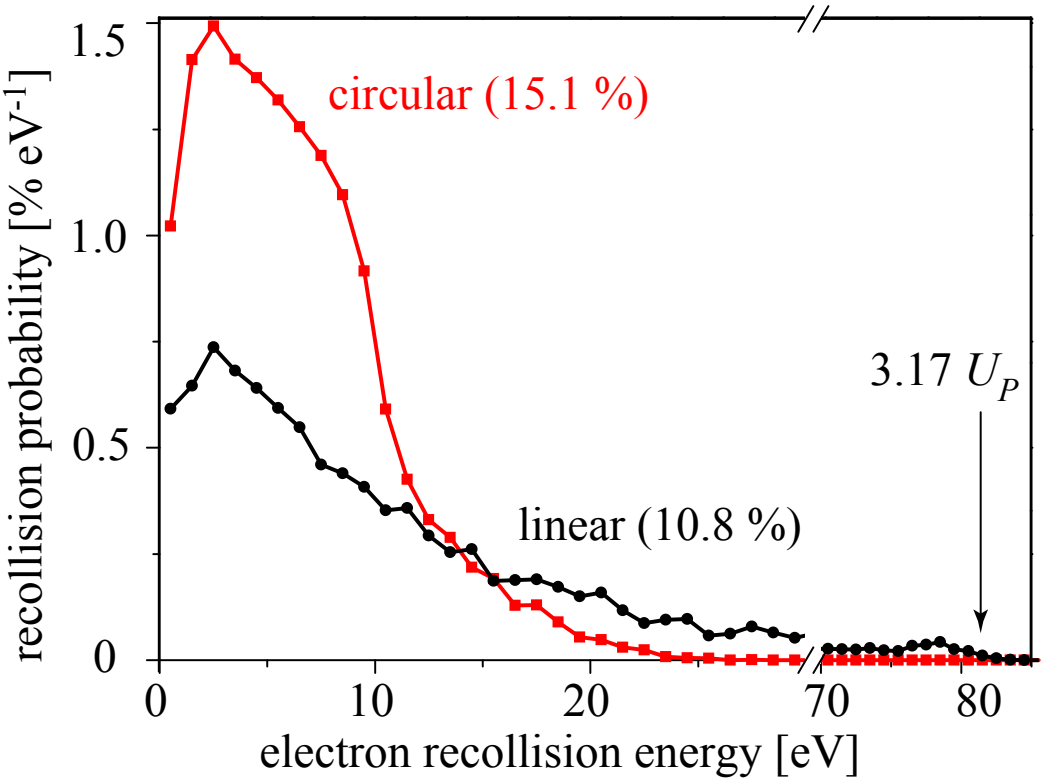

Figure 8.14: Probability to find different recollision energies for electrons emitted from the inner $(0.65a)$ *and outer radius* $(1.00a)$ *of the* C_{60} *molecule in linearly or circularly polarised light at* $I = 4.3 \times 10^{14}\ W/cm^2$, $797\,nm$. *Initial conditions (at* $t = 0$*) are taken statistically: laser field phase* $0 \leq \varphi < 2\pi$, *electron starting radius* $0.65a$ *or* $1.00a$, *electron kinetic energy* $0 \leq W_{in} \leq 10\,eV$ *(radial emission) at* $0 \leq \Phi < 2\pi$ *and* $0.95\pi/2 \leq \Theta \leq \pi/2$.

distribution of the following parameters: laser field phase $0 \leq \varphi < 2\pi$, electron starting radius $0.65a$ or $1.00a$, electron kinetic energy $0 \leq W_{in} \leq 10\,\text{eV}$ (radial emission) at $0 \leq \Phi < 2\pi$ and $0.95\pi/2 \leq \Theta \leq \pi/2$. The results generated from this statistical test are represented in Fig. 8.14. This histogram shows electron recollision probability plotted as a function of its kinetic energy at the moment of recollision for circularly (red squares) and linearly (black circles) polarised radiation at $I = 4.3 \times 10^{14}\,\text{W/cm}^2$ and $797\,\text{nm}$. About 15% of the trajectories return in circularly polarised light, while only 11% recollide for linear polarisation. On the other hand, there is still a small, but non negligible number of trajectories in linearly polarised light which return with much higher energies – up to the well known value of $3.17U_P$ as indicated in Fig. 8.14, while trajectories in circularly polarised light only harvest up to $25\,\text{eV}$.

It should be pointed out that this trajectory study is not intended to give a quantitative or even qualitative explanation for the experimentally observed enhancement of fragments

created by circularly polarised light over those excited by linearly polarised light at high laser intensities. This is not to be expected from a single electron trajectory study in a situation, when multielectron dynamics dominates. A key point here is just to illustrate that the general believe about circular polarisation being unable to lead to energy deposition due to recollision is not necessarily true for extended systems and strong laser fields. A more sophisticated calculation in the spirit of those done for rare gas clusters [SSR06] may lead to interesting results, when the ionising field is circular rather than linear. In view of the examples of the trajectories shown in Fig. 8.13 one may very well imagine a vehement collective motion and collisions in a many electron system driven by circularly polarised strong laser fields. This certainly could lead to substantial heating of the electron gas and subsequently of the nuclear backbone which is then finally probed by fragmentation long after the laser pulse is over (see Sec. 9.4).

8.3.2 Photoelectron Spectroscopy

At high laser intensities multiphoton ionisation occurs via above threshold ionisation (ATI), when an atom or molecule exposed to intense femtosecond laser radiation absorbs more photon than required for ionisation (see Sec. 3.2). The corresponding photoelectron spectrum has to exhibit peaks separated by the laser photon energy $\hbar\omega_0$. The envelope of ATI peaks in the photoelectron spectrum does not decrease regularly, but shows plateau region, where its intensity stays roughly constant or even increases with peak number [PNX94] due to recollision of photoelectrons on their parent ion [BLK94]. Such recollisions can produce electrons with kinetic energies above $2U_P$ [PBN94, WSK96]. Therefore, if the recollision process is influenced by the laser light ellipticity, this must be reflected in plateau region of mass spectra measured with different ellipticity.

To see recollision fingerprints in photoelectron spectra of C_{60} several spectra were recorded as a function of the laser light ellipticity. As an example, Fig. 8.15 shows two photoelectron spectra obtained with the laser intensity of $1.4 \times 10^{14}\,\mathrm{W/cm^2}$ for linear and circular polarised light. Both photoelectron spectra show ATI peaks up to the kinetic energy of $\simeq 13\,\mathrm{eV}$ ($\simeq 1.6U_P$). The observed Rydberg structure [BHS01] on top of the first ATI peak is shown in the enlarged insert. This structure arises from the AC-Stark shift (see Sec. 3.2) of Rydberg states producing multiphoton resonances with the laser frequency. Each peak appears at a fixed

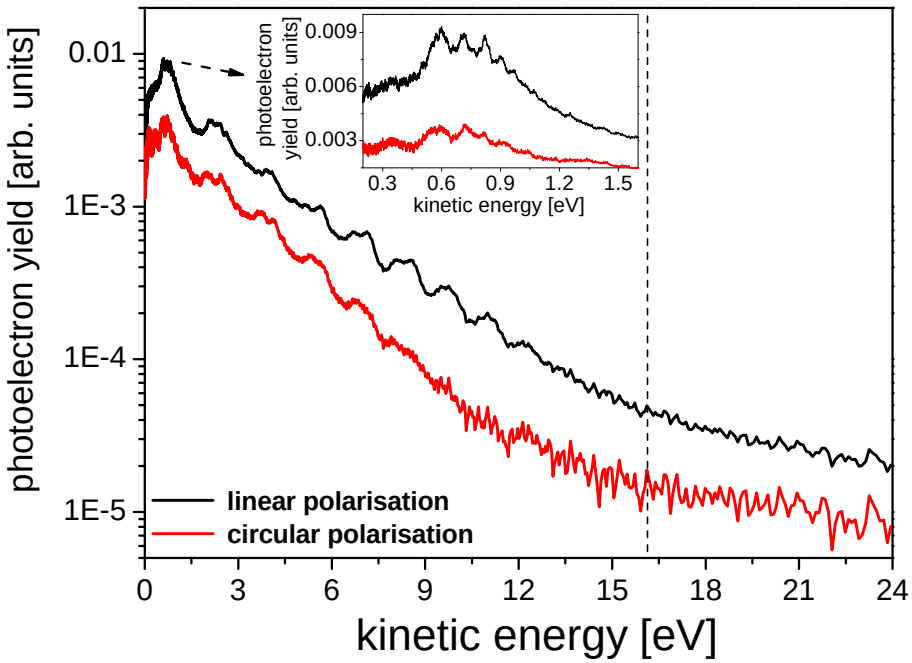

Figure 8.15: Photoelectron spectra of C_{60} obtained with laser intensity of 1.4×10^{14} W/cm^2 for linear (black line) and circular (red line) light polarisations. Insert demonstrates Rydberg states on top of the first ATI peak. Dashed vertical line indicates $2U_P = 16.1\,eV$.

kinetic energy corresponding to the precise intensity at which this level shifts into resonance with the laser. There is no any essential difference between these two photoelectron spectra in the photoelectron energy range above $2U_P = 16.1$ eV. But the photoelectron signals in this range are very weak and noisy and ATI structure is not visible at any light ellipticity. Therefore, the experimental data obtained under present experimental conditions can not definitely indicate presence or absence of recollisions.